

Methods

Subcellular dynamics studies of iron reveal how tissue-specific distribution patterns are established in developing wheat grains

Sadia Sheraz¹, Yongfang Wan² , Eudri Venter³ , Shailender K. Verma⁴ , Qing Xiong⁴, Joshua Waites^{4,5} , James M. Connorton^{4,5} , Peter R. Shewry² , Katie L. Moore¹  and Janneke Balk^{4,5} 

¹School of Materials and Photon Science Institute, University of Manchester, Manchester, M13 9PL, UK; ²Department of Plant Sciences, Rothamsted Research, Harpenden, AL5 2JQ, UK;

³Bioimaging facility, Department of Computational and Analytical Sciences, Rothamsted Research, Harpenden, AL5 2JQ, UK; ⁴Department of Biological Chemistry, John Innes Centre,

Norwich, NR4 7UH, UK; ⁵School of Biological Sciences, University of East Anglia, Norwich, NR4 7TJ, UK

Summary

Author for correspondence:
Janneke Balk
Email: janneke.balk@jic.ac.uk

Received: 3 February 2021
Accepted: 14 April 2021

New Phytologist (2021)
doi: 10.1111/nph.17440

Key words: aleurone, iron, NanoSIMS, nicotianamine, pulse-chase, trafficking, wheat.

- Understanding the mechanisms of iron trafficking in plants is key to enhancing the nutritional quality of crops. Because it is difficult to image iron in transit, we currently have an incomplete picture of the route(s) of iron translocation in developing seeds and how the tissue-specific distribution is established.
- We have used a novel approach, combining iron-57 (⁵⁷Fe) isotope labelling and nanoscale secondary ion mass spectrometry (NanoSIMS), to visualize iron translocation between tissues and within cells in immature wheat grain, *Triticum aestivum*.
- This enabled us to track the main route of iron transport from maternal tissues to the embryo through the different cell types. Further evidence for this route was provided by genetically diverting iron into storage vacuoles, with confirmation provided by histological staining and transmission electron microscopy energy dispersive X-ray spectroscopy (TEM-EDS). Almost all iron in both control and transgenic grains was found in intracellular bodies, indicating symplastic rather than apoplastic transport. Furthermore, a new type of iron body, highly enriched in ⁵⁷Fe, was observed in aleurone cells and may represent iron being delivered to phytate globoids.
- Correlation of the ⁵⁷Fe enrichment profiles obtained by NanoSIMS with tissue-specific gene expression provides an updated model of iron homeostasis in cereal grains with relevance for future biofortification strategies.

Introduction

As widely consumed staple crops, cereals are important sources of mineral micronutrients, including iron and zinc which are essential for human health. However, deficiencies in these minerals affect large parts of the global population (WHO, 2013, 2015). The daily requirements for bioavailable iron and zinc are often not met in cereal-based diets for two reasons. First, iron and zinc are unevenly distributed in the grain, accumulating at high concentrations in the embryo (germ) and outer layers (bran), which are removed during polishing or milling. By contrast, both minerals are low in the starchy endosperm which constitutes about 70% of the grain and is preferentially consumed in human diets (as white wheat flour and polished rice, for example). Second, most of the iron and zinc in the embryo and aleurone layer is bound to phytic acid, forming insoluble complexes that have poor bioavailability. Attempts to biofortify cereal grains are focussing on increasing the total amounts of iron and zinc, changing their distribution and reducing phytic acid levels (Vasconcelos *et al.*, 2017; Cominelli *et al.*, 2020).

The molecular pathways of iron and zinc uptake from the soil into plant roots are relatively well understood, but we know little about mineral loading into the seeds and subsequent distribution to different tissues (Mari *et al.*, 2020). Recent isotope labelling studies in Arabidopsis suggested that virtually all the iron in seeds was remobilized from senescing leaves (and other organs) with only an indirect contribution from uptake by the roots (Pottier *et al.*, 2019). Studies using isotope pulse labelling have not yet been conducted in wheat, but a time course of mineral partitioning indicated that 77% of the iron in mature grain is remobilized from the shoot (Garnett & Graham, 2005), and that this process is regulated by NAC transcription factors (Uauy *et al.*, 2006; Waters *et al.*, 2009; Borrill *et al.*, 2019).

Physical separation between the tissues of the mother plant and the seed (the filial generation) means that iron is secreted and then taken up again by the developing zygote (Mari *et al.*, 2020). Nutrients are delivered to the developing grain via the vascular bundle which runs through the ventral crease in wheat, and the nucellar projection. The latter is all that remains from the nucellus which

once surrounded the embryo sac, and comprises a dense group of transfer cells along the top of the vascular bundle (see Bechtel *et al.* (2009) for a description of wheat grain development). In the early stages of grain development, nutrients are secreted from the maternal transfer cells into a cavity that will fill up as the endosperm of the developing seed expands. The rapidly dividing endosperm cell mass differentiates into specialized cell types (Olsen, 2020), most notably a single outer layer of aleurone cells which differ from the other endosperm cells in lacking starch and accumulating protein, lipids, minerals and phytic acid. Periclinal divisions of the aleurone cells continue to form several layers of subaleurone cells which accumulate protein but not minerals. The aleurone cells that are in contact with the nucellar transfer cells in the tip of the crease differentiate to have a special function in nutrient transport. For this reason they are often called endosperm transfer cells, but to avoid confusion with the nucellar transfer cells we will use the term modified aleurone here, which is also commonly used in the literature (Evers, 1970; Borg *et al.*, 2009).

The distribution of iron in biological materials has been visualized using histological staining, X-ray fluorescence (XRF), micro-proton induced X-ray emission (μ -PIXE) and laser-ablation inductively coupled plasma mass spectrometry (LA-ICP-MS). When applied to cereal grains, these techniques showed accumulation of iron in the crease, the aleurone layer and the scutellum of the embryo in wheat (Neal *et al.*, 2013; Singh *et al.*, 2013; De Brier *et al.*, 2016) and a similar pattern in other cereals (Takahashi *et al.*, 2009; Iwai *et al.*, 2012; Detterbeck *et al.*, 2020). Nanoscale secondary ion mass spectrometry (NanoSIMS) has also become a significant tool to visualize minerals at the subcellular level due to its unique capabilities of high spatial resolution (50 nm), high sensitivity (ppm and ppb for some elements) and detection of trace elements and isotopes (for example see Malherbe *et al.*, 2016; Kopittke *et al.*, 2020). During NanoSIMS analysis, the sample surface is impacted with a high-energy primary ion beam which causes sputtering of the surface and ejection of atoms and small molecules. Some of this sputtered material becomes ionized, referred to as 'secondary ions', which are detected and analysed by mass in a double focussing mass spectrometer. The instrument has two primary ion sources to generate either a caesium ion (Cs^+) beam, used for analysis of negative secondary ions, or an oxygen ion (O^-) beam to analyse positive secondary ions. Due to the design of the NanoSIMS, the secondary ions must have an opposite polarity to the primary ions. Up to seven secondary ions can be detected simultaneously but these must be selected before acquiring the data (Hoppe *et al.*, 2013). As the NanoSIMS operates under ultra-high vacuum, careful sample preparation is required to avoid redistribution of elements from their *in vivo* location (Grovenor *et al.*, 2006).

Very few genes have been characterized to date that influence the distribution pattern of iron in seeds. One of those is the vacuolar iron transporter (VIT). Disruption of this gene in Arabidopsis resulted in relocation of iron from provascular strands to the abaxial (lower) epidermis in the embryo which occupies most of the seed volume (Kim *et al.*, 2006). In rice, mutation of either the *VIT1* or *VIT2* paralogue leads to iron accumulation in the embryo and depletion in the large endosperm of the grain (Zhang *et al.*, 2012; Bashir *et al.*, 2013; Che *et al.*, 2021)

Conversely, overexpression of *TaVIT2* in the starchy endosperm of wheat grain leads to iron accumulation in this tissue and > two-fold more iron in white flour (Connorton *et al.*, 2017).

Many questions remain regarding the mechanisms that determine how iron is translocated from the maternal vascular bundle into the developing seed and how this element is distributed within the seed as tissues differentiate and expand. To address these questions, we combined iron isotope labelling with NanoSIMS to compare the dynamics of iron distribution in developing wheat grains between a control and a *TaVIT2* overexpressing line. Our results revealed that the major route of iron is from the nucellar transfer cells through a zone of endosperm cells between the crease and the embryo, but that this pathway is disrupted by overexpression of *TaVIT2*. Different cell types displayed specific patterns of isotope-enriched vesicles and globoids, highlighting the different roles of each cell type in iron translocation.

Materials and Methods

Plant material and growth

Transformation of wheat lines (*Triticum aestivum* var. Fielder) with pBract202-TaVIT2 and their initial characterization have been described in the literature (Connorton *et al.*, 2017; Hayta *et al.*, 2019). As a control, we used the offspring of a plant regenerated after transformation that tested negative for the transgene. This line, 22-15, did not accumulate iron in the endosperm and white flour fraction (Supporting Information Table S1; Connorton *et al.*, 2017). All analyses were carried out using the T3 generation, except for the germination tests for which T4 grain was used. Plants were grown in a glasshouse kept at approximately 20°C with 16 h of light. Plants were watered as required.

T-DNA copy number and TAIL-PCR

To estimate the numbers of T-DNA copies in individual plants, quantitative real time polymerase chain reaction (PCR) analysis was carried out similar to the approach taken by (Bartlett *et al.*, 2008) using DNA from seedlings of the T4 generation. Thermal asymmetric interlaced (TAIL) PCR was performed essentially as described in Wu *et al.* (2015), except that recombinant *Taq* polymerase purified from *Escherichia coli* was used (Engelke *et al.*, 1990). All primers used are listed in Table S2.

Element analysis by ICP-OES and ICP-MS

Preparation of flour fractions and element analysis were essentially carried out as previously described (Tosi *et al.*, 2011; Connorton *et al.*, 2017). See Supporting Information Methods S1 for details.

Isotope labelling and sample preparation for microscopy

Iron-57 in the form of $^{57}\text{Fe}_2\text{O}_3$ (Cambridge Isotope Laboratories, Tewksbury, MA, USA) was added to a small volume of

concentrated hydrochloric acid and incubated at 37°C overnight until it was dissolved. The solution was diluted with water (H₂O) to obtain 20 mM ⁵⁷Fe in 1 M hydrochloric acid (HCl) and stored at 4°C. The ⁵⁷Fe feeding solution (50 μM ⁵⁷Fe, 0.5 mM sodium citrate and 10 mM MES-KOH pH 6.0) was freshly prepared by mixing 25 μl ⁵⁷Fe-HCl stock solution, 50 μl 100 mM sodium citrate, 10 μl 1 M sodium hydroxide and 1 ml 100 mM MES buffer, made up to a final volume of 10 ml with H₂O. After adjusting the pH to 6.0, 1 ml was filtered (pore size 0.22 μm) and pipetted into a 1.5-ml Eppendorf tube attached to the ear with tape. A 10 μl glass microcapillary tube (Drummond, Sigma Aldrich, St Louis, MO, USA) was placed in the tube and the other end was inserted into the rachis (see Fig. 3a and Supporting Information Methods S1). The solution was taken up naturally by the wheat ear over the course of *c.* 12 h. The grains (40–50) from one ear were harvested after 24, 72 or 240 h and dissected into four parts: embryo, and three equal remaining sectors (S1, S2 and S3), and then were freeze-dried for ICP-MS. Four grains from the middle of the ear were harvested for high pressure freezing, sectioning and microscopy.

Transverse slices of the grain (0.1 mm thick, see Fig. 3 for positions) were infiltrated with 0.5 M MES-KOH pH 5.4, and frozen using a high-pressure freezer (HPM 100; Leica Microsystems, Milton Keynes, UK). Freeze substitution, embedding in LR White resin (R1281; Agar Scientific, Stansted, UK) and sectioning was as described in Moore *et al.* (2012, 2016).

Iron staining using the Perls' method

Iron staining of tissue was performed as described in the literature (Meguro *et al.*, 2007; Roschztardtz *et al.*, 2009) using the Perls' method, enhanced with 3,3'-diaminebenzidine where indicated.

Transmission electron microscopy energy dispersive X-ray spectroscopy (TEM-EDS) analysis

The embedded wheat grain samples used for NanoSIMS were sectioned with a Leica UC7 ultramicrotome (Leica Microsystems, Vienna, Austria), and 100-nm ultrathin sections were mounted on 200-mesh copper TEM grids (Agar Scientific). Where indicated, sections were contrasted with 2% uranyl acetate for 10 min, and Reynolds' lead citrate (Reynolds, 1963) for 2 min. Transmission electron microscopy (TEM) imaging was done with a 200 kV Jeol 2011 TEM (Jeol Ltd, Tokyo, Japan). Circular regions of interest were chosen for energy dispersive X-ray spectroscopy (EDS) analysis. X-rays were detected with an Oxford INCAx-sight detector (Oxford Instruments, Abingdon, UK), and analysed with the Oxford INCA SUITE v.4.02.

Nanoscale secondary ion mass spectrometry (NanoSIMS)

NanoSIMS analysis was performed with a Cameca NanoSIMS 50L (Cameca, Gennevilliers, France), explained in detail elsewhere (Hoppe *et al.*, 2013). A 16 keV O⁻ beam with a current between 45 and 85 pA and a beam size of approximately 600 nm (L1 = 1300–1582, D1 = 2) (300 μm aperture) was focussed onto

the sample and rastered over the surface to generate positive secondary ions. The L1 lens was used to increase the beam current and counts of ⁵⁷Fe, and reduce analysis time, but this resulted in a lower spatial resolution than can typically be achieved with the NanoSIMS (100 nm). The entrance slit was set to position 3 (20 μm width), and the aperture slit to position 2 (200 μm width).

The detectors were aligned to simultaneously detect ²³Na⁺, ³¹P⁺, ⁴⁰Ca⁺, ³¹P¹⁶O⁺, ⁵⁶Fe⁺ and ⁵⁷Fe⁺. Detectors were aligned using bulk standards and particular care was taken to minimize the mass interference of ⁵⁶Fe¹H⁺ with ⁵⁷Fe⁺ (Supporting Information Fig. S7). Before analysis of regions of interest, a depth profile was acquired from a bulk iron standard to check the measured ⁵⁷Fe : ⁵⁶Fe isotope ratio and compare it to the natural isotope ratio of 2.3%. The detector for ⁵⁷Fe was set slightly to the left of the centre of the peak to avoid the mass interference of ⁵⁶Fe¹H⁺. This resulted in a slightly lower measured isotope ratio than natural, with an average of 2.24% across all measurements (Fig. S7c). All regions of interest and subcellular features were however enriched by significantly more than the 0.06% difference in the ratio.

Regions of interest were selected using the charge-coupled device (CCD) camera on the NanoSIMS. The samples were coated with 40 nm of platinum (Pt) before loading into the instrument to minimize sample charging. The Pt was removed by repeatedly scanning a defocussed O⁻ beam (D1 = 0) over an area of 70 μm × 70 μm with a total dose of 2.55 to 3 × 10¹⁷ ions/cm⁻². Following implantation, ion images were acquired using a focussed beam over an area of 50 μm × 50 μm with 256 × 256 pixels and dwell time of 2000 μs per pixel. Several hundred images of each region of interest were acquired and summed together to improve the statistics.

Data processing was conducted with FIJI software using the OpenMIMS plugin (Harvard, Cambridge, MA, USA). Image processing included drift correction, summing of images, selecting regions of interest (ROIs) and extracting counts from them and generating colour merge and hue saturation intensity (HSI) ratio images to show isotopic variation of ⁵⁷Fe : ⁵⁶Fe.

Bioinformatics

Iron homeostasis genes in wheat were taken from (Borrill *et al.*, 2014) and supplemented with literature searches to a total of 232 genes including homeologues. Publicly available RNA-sequencing (RNA-Seq) datasets of modified aleurone, starchy endosperm and aleurone layer enriched samples (Pfeifer *et al.*, 2014) were mapped to the IWGSC RefSeq v.1.1 gene models using KALLISTO v.0.43.1 (Bray *et al.*, 2016). Gene expression was analysed using the R package SLEUTH v.0.30.0 with default settings. This identified 213 transcripts from 67 wheat iron homeostasis genes that were expressed in at least one tissue. Transcript per million (TPM) means ± SD were calculated from four replicates in the RNA-Seq data set. To filter for real expression over noise, a cut-off of 1 TPM in at least one tissue was imposed, and a *q*-value of significance < 0.05 as calculated using the likelihood ratio test.

Statistical analysis

Statistical analysis was carried out using the software packages GRAPHPAD or EXCEL.

Results

Genetic characterization of *HMW-TaVIT2* line 22-19 for further study

Previously we generated 25 independent *Agrobacterium*-transformed wheat lines with one or more copies of the *HMW-TaVIT2* transgene, placing *TaVIT2* under the control of the starchy endosperm-specific promoter of the gene *High Molecular Weight subunit of glutenin 1Dx5* (Connorton *et al.*, 2017). Transcript levels of *TaVIT2* in developing grain correlated well with the number of transgene copies (factor 0.2, $R^2 = 0.597$, $P < 0.01$). By contrast, the iron concentration in hand-milled flour was variable between lines with similar transgene copy numbers. To select one line for detailed study, we chose line 22-19 based on a representative pattern of iron staining in hand-dissected grain and a consistent > two-fold increase in the iron concentration in the white flour fraction. T-DNA copy number analysis of the T1 generation indicated that line 22-19 had more than one insert of tandemly arranged T-DNAs. Further selection gave a stable pattern of 8 to 10 T-DNA copies in the T2, suggesting the line was homozygous for a tandem array of four copies and possibly heterozygous for another single copy insertion (Table S1).

To determine the position of the T-DNA insertion(s), TAIL-PCR was performed with nested primer sets for either the left border (LB) or right border (RB) T-DNA sequence, in combination with an arbitrary degenerate (AD) primer. A 1.1-kb PCR product generated with the LB primer set and the AD3 primer was found consistently in transgenic plants but not in the non-transgenic control. Part of the sequence of the PCR product matched the LB and the other part matched the 5'UTR of *TraesCS4D02G046700* (Fig. S1a,b). No specific PCR products were generated with the RB primer set with any of the four AD primers. The position of the T-DNA was verified with primers spanning the insertion site and the LB3 primer (Fig. S1c). Analysis of DNA from 12 T1 siblings showed that the selected line (22-19-4) was homozygous for this T-DNA insertion, in agreement with the segregation pattern of T-DNA copies in the T2 generation.

TraesCS4D02G046700 encodes a Ubc enzyme variant (Uev), belonging to a small gene family conserved in all eukaryotes. The closest rice homologue is *OsUEV1A* (*Os03g0712300*) which has 85% amino acid identity (Wang *et al.*, 2017). Transcript levels of the wheat *UEV1A-4D* gene are slightly increased in developing grain, but this was also the case for the 4A and 4B homologues (Fig. S1d). Moreover, the wheat *UEV1A-4A* and *-4D* homologues are identical in amino acid sequence and have highly similar expression patterns (expVIP database, wheat-expression.com). Thus, the T-DNA insertion in line 22-19 does not appear to disrupt the expression of an essential gene.

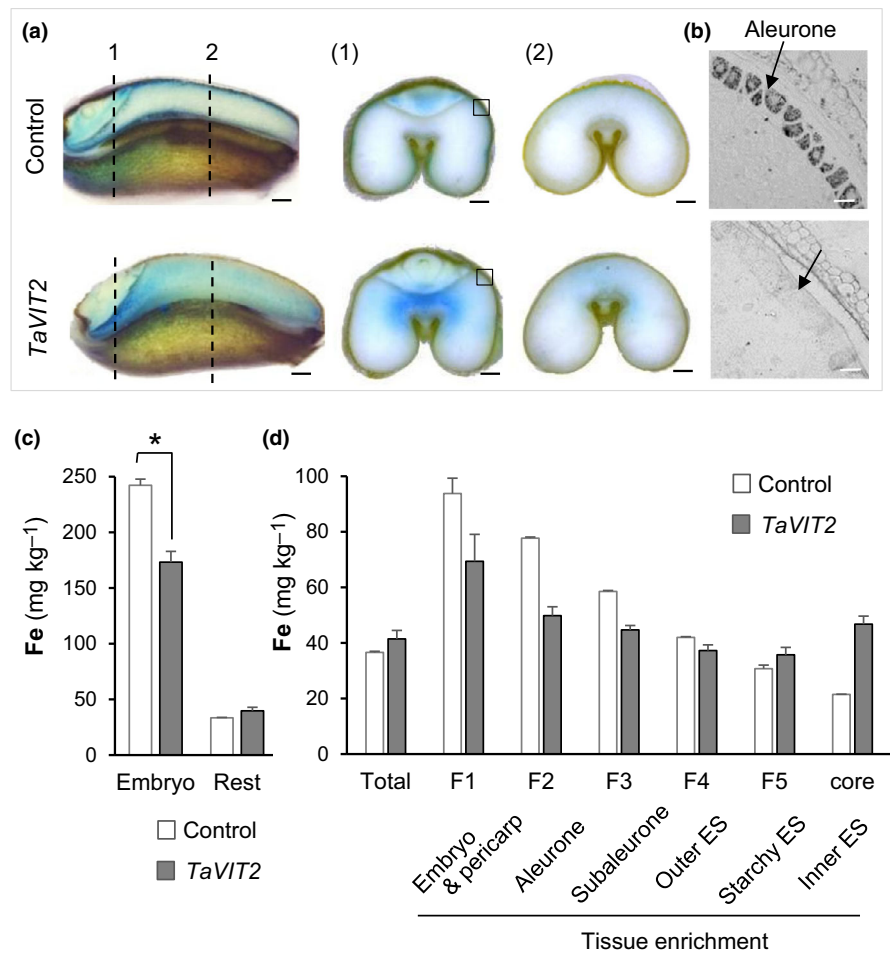
In *TaVIT2* grain, the amount of iron is increased in a specific region of the endosperm and decreased in the embryo and aleurone cells

To further investigate differences in iron distribution as a consequence of overexpressing *TaVIT2* in the endosperm, T3 grains from line 22-19-4-5 (henceforth called *TaVIT2*) and from control plants were cut longitudinally and at two transverse positions before staining with Perls' reagent (Fig. 1). Similar to other *TaVIT2* transformation events (Connorton *et al.*, 2017), dense iron staining was found in the starchy endosperm surrounding the crease. Iron staining in this part of the endosperm was more intense in the proximal region close to the embryo than in the distal region (Fig. 1a, compare transverse section 1 and 2), in a zone of cells equivalent to the endosperm adjacent to scutellum (EAS) in maize kernels (Doll *et al.*, 2020). By contrast, both the embryo and aleurone layer in *TaVIT2* grain displayed a lower intensity of iron staining than in control grain. The difference in iron staining of the aleurone was also observed in higher magnification images using diamine benzidine (DAB)-enhanced Perls' staining (Fig. 1b).

To quantify the decrease in iron content in the embryos, developing grains at 24 d post anthesis (dpa) were hand-dissected into two parts, embryo and the remaining tissues (rest), and the concentration of iron was measured by ICP-MS. Iron was significantly decreased, by 28.5%, in embryos of *TaVIT2* grains compared to control embryos, with a concentration of $173 \pm 20 \text{ mg kg}^{-1}$ dry weight compared to $242 \pm 9 \text{ mg kg}^{-1}$ in control ($P > 0.03$, see Fig. 1c). However, germination tests of *TaVIT2* grain showed no effect on germination or on early seedling growth in alkaline soil (Fig. S2).

The iron contents of the aleurone layer and endosperm of mature grains were estimated by analysis of pearling fractions. This technique uses abrasion to remove material from the outer layers to the inner core of the grain. Sequential cycles of pearling result in fractions enriched in embryo and pericarp (F1), aleurone (F2) and subaleurone (F3). The iron concentration in the F1 fraction of *TaVIT2* grain was decreased by 26% compared to control grain, in agreement with the percentage decrease in dissected embryos. It should be noted that the absolute iron concentration in the F1 pearling fraction is much lower than in dissected embryos, because of dilution by dry matter from the bran and the embryo at maturity. The F2 fraction contained 36.6% less iron in *TaVIT2* grain, $49.8 \pm 3.2 \text{ mg kg}^{-1}$ dry weight compared to $77.7 \pm 0.4 \text{ mg kg}^{-1}$ in control grain (Fig. 1d). The inner starchy endosperm (core) contained approximately two-fold more iron in *TaVIT2* grain, whereas the iron concentration in the whole grain is similar in *TaVIT2* and control grain, as noted previously (Connorton *et al.*, 2017; Balk *et al.*, 2019). The distribution of other metals such as manganese and zinc were little affected by *TaVIT2* overexpression, except for small increases in the F1 fraction (Fig. S3). The distribution of phosphorus in *TaVIT2* grain was not affected, resulting in a lower phosphorus : iron ratio in the core of the endosperm (Fig. S3). Thus, overexpression of *TaVIT2* in the endosperm does not affect the amount of iron mobilized from the maternal plant into the grain,

Fig. 1 Distribution of iron in developing wheat grains overexpressing *TaVIT2* in the endosperm and nontransformed control. (a) Grains were harvested 24 d post anthesis (dpa), hand-sectioned and stained for iron (blue) using the Perls' staining method. The dashed lines (1, 2) in the longitudinal sections on the left indicate the positions of the transverse sections on the right. Bars, 0.5 mm. (b) Thin sections of embedded material were stained with enhanced Perls'-staining. The grey-scale images show part of the aleurone cell layer marked by the square in (a), (1). Bars, 50 μ m. (c) Iron concentration per unit dry weight determined by inductively coupled plasma mass spectrometry (ICP-MS). Embryos were hand-dissected from grains at 22–25 dpa. Values represent the mean \pm SE of three biological replicates, which are pools of 40 to 50 embryos from one ear. *, $P < 0.05$, Student *t*-test. (d) Fractions obtained by pearling of mature grain were analysed for iron concentration (shown here) and other elements (Supporting Information Fig. S3) by inductively coupled plasma optical emission spectroscopy (ICP-OES). Values represent the mean of two biological replicates of 30 g grain. Error bars represent half the difference between the measurements. The tissue enrichment in each fraction is taken from Tosi *et al.* (2018).



but does affect the distribution of iron within the grain: iron accumulates in a specific region of the endosperm at the expense of iron translocation to the embryo and aleurone.

TaVIT2 endosperm cells accumulate iron in clusters of vesicles and globoids

Based on its function as a vacuolar iron transporter, overexpression of *TaVIT2* is expected to lead to iron accumulation in vacuoles. To obtain information on the subcellular location of iron in *TaVIT2* grain, semi-thin transverse grain sections were stained with Perls'-DAB (Fig. 2). Dense granules of dark staining were observed in the endosperm of *TaVIT2* grain, but not in control grain (Fig. 2a,b). The region where intense iron staining was found corresponded with the blue Perls' staining in hand-cut sections of *TaVIT2* grain (Fig. 1a). Higher magnification images showed that the iron staining was confined to clusters of small round bodies of approximately 0.5–2 μ m in diameter in the cytoplasm of endosperm cells (Figs 2c, S4). There appeared to be no association with other cell organelles, such as starch grains or the nucleus.

TEM identified several distinct electron-dense morphological structures in the endosperm region of interest in *TaVIT2* grain, which were absent from control grain. The most abundant

morphologies were particles forming the outline of vesicles 0.2–0.8 μ m in diameter but lacking any trace of a membrane (Fig. 2d,f); and clusters on the outside of membrane-bound vesicles 0.5–2.3 μ m in diameter (Figs 2e, S5). Dispersed particles and aggregates of smaller particles were also observed but were less abundant (Fig. S5a). Elemental analysis by EDS indicated that all four electron-dense morphologies in *TaVIT2* grain contained iron, whereas iron was not detectable outside these areas (Fig. S5). The two most abundant types of iron-rich morphologies seen in TEM were also distinguishable by NanoSIMS (Fig. 2e,f). The NanoSIMS images were aligned with Perls'-DAB staining applied to adjacent sections. While the two morphologies looked identical with Perls'-DAB staining, this technique revealed that the smaller type are surrounded by an intracellular membrane (Fig. 2f, white arrow), indicating they are iron globoids inside a larger vacuole.

Accumulation of iron in a specific region of the starchy endosperm but not throughout, raises the question whether this coincides with a local abundance of iron or is due to localized expression of the *TaVIT2* transgene. The *TaVIT2* transgene is expressed using the *HMW Glu-1Dx5* promoter, which is active in the entire starchy endosperm during grain filling as shown by promoter-GUS studies (Lamacchia *et al.*, 2001). To verify that the expression pattern of *HMW-TaVIT2* is similar, we carried

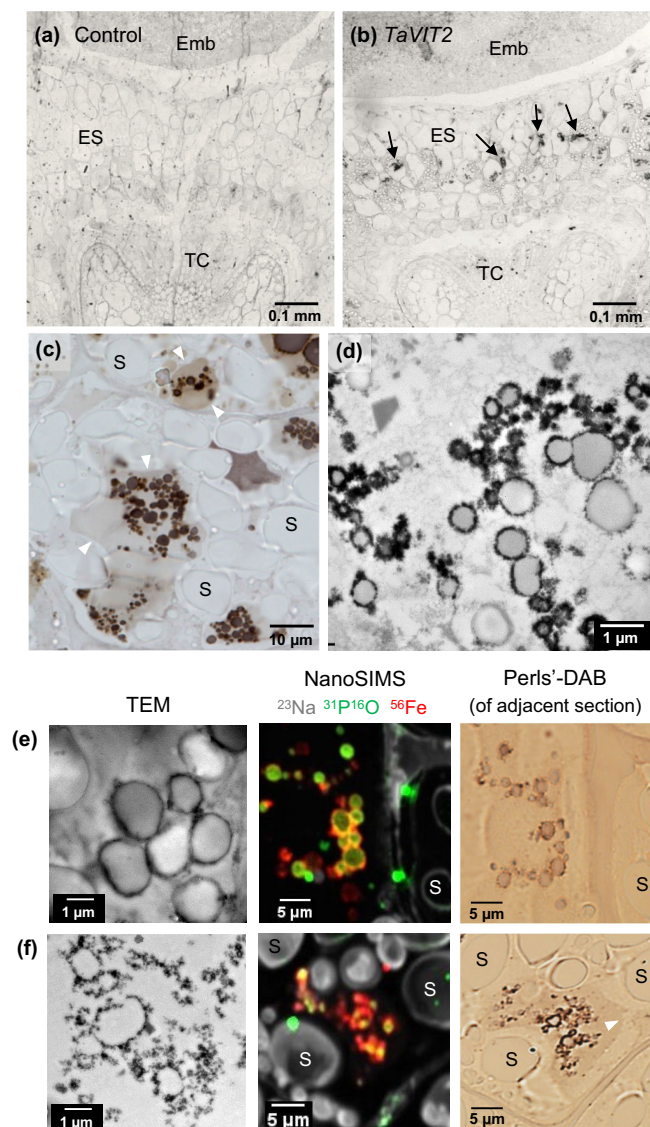


Fig. 2 Iron accumulates in subcellular clusters in *TaVIT2* endosperm cells. (a, b) Transverse sections of wheat grains (21 d after anthesis) from (a) control and (b) *TaVIT2* stained for iron using the enhanced Perls' method. Emb, embryo; ES, endosperm; TC, transfer cells of the nucellar projection. Black arrows point to iron accumulated in clusters. (c) Detail of endosperm cells in *TaVIT2* grain stained for iron, imaged with differential interference contrast (DIC) microscopy. S, starch grain. (d) Electron-dense structures in endosperm cells of *TaVIT2* grain, imaged by transmission electron microscopy (TEM). (e, f) Subcellular structures in (b) containing iron imaged by TEM (and energy dispersive X-ray spectroscopy (EDS), see Supporting Information Fig. S5), nanoscale secondary ion mass spectrometry (NanoSIMS) and Perls'-diamine benzidine (DAB) staining. The NanoSIMS and Perls'-DAB images are from adjacent 1 μm sections. White arrowhead indicates the boundary of the vacuole.

out *in situ* hybridizations of 21 dpa grain. Hybridization with an antisense *TaVIT2* probe showed intense positive staining in all parts of the endosperm of *TaVIT2* grain, especially in the sub-aleurone cells, matching the expected pattern of *HMW Glu-1Dx5* promoter activity. In control grain, positive staining but of weaker intensity was seen in the aleurone cell layer, where endogenous *TaVIT2* is expressed. There was no signal in any

tissue with the sense probe which served as negative control (Fig. S6).

In summary, accumulation of iron-dense vesicles, representing iron trapped by overexpression of *TaVIT2*, indicates that the starchy endosperm region between the maternal transfer tissue and the embryo is a major transport route of iron in developing wheat grain.

The rate of iron transport to the embryo is decreased in *TaVIT2* grain

To study how iron is translocated into the developing grain at (sub)cellular resolution, we designed an experimental protocol for iron isotope labelling and subsequent NanoSIMS analysis (Fig. 3a). Iron-57 (^{57}Fe) was chosen as a stable isotope over iron-54 and iron-58 because its mass differs sufficiently from other abundant elements in biological material and it has a relatively low natural abundance of 2.12%. By contrast, iron-54 has a natural abundance of 5.8% which would make it harder to detect enrichment after pulse-labelling. Although iron-58 has a very low natural abundance (0.28%) it is difficult to separate from nickel-58 (68.1% natural abundance) by mass. To detect iron by NanoSIMS, previously we used the caesium ion (Cs^+) beam to detect FeO^- (Moore *et al.*, 2012), but the mass of $^{57}\text{Fe}^{16}\text{O}^-$ is nearly indistinguishable from the $^{56}\text{Fe}^{16}\text{O}^{1}\text{H}^-$ ion. However, the positive ions $^{57}\text{Fe}^+$ ($m/z = 56.9354$) and $^{56}\text{Fe}^{1}\text{H}^+$ ($m/z = 56.9428$), generated with the oxygen ion (O^-) beam, are sufficiently separated to allow reliable mapping of the $^{57}\text{Fe}^+$ signal (Fig. S7).

To directly target the iron isotope to the developing grains, a 1 ml solution of 50 μM $^{57}\text{Fe}^{3+}$ and 0.5 mM citrate was fed into the base of the rachis (stem of the flowering spike) using a glass microcapillary tube (Fig. 3a). Feeding was performed on wheat ears around 18 dpa, to coincide with the mid-stage of grain filling and iron mobilization (Waters *et al.*, 2009; Beasley *et al.*, 2019), and high activity of the *HMW* promoter driving expression of *TaVIT2* (Lamacchia *et al.*, 2001). Following a 12 h isotope feeding pulse, the optimal chase time was determined experimentally, by ICP-MS measurement of ^{57}Fe in the embryo and rest of the grain at 24, 72 and 240 h (10 d), counting from the start of feeding. The relative abundance of ^{57}Fe increased from background levels (2.12%) to *c.* 5% after 24 h and to *c.* 8% after 72 h (Fig. 3b). Sampling the grain 10 d after isotope labelling showed no further increase in ^{57}Fe enrichment, either because the grain filling period had come to an end or because nonlabelled iron from the senescing leaves was mobilized at a sufficient rate to dilute the remaining isotope. Capillary insertion had no significant effect on grain development (Moore *et al.*, 2016) and the total iron concentration in 'fed' and 'nonfed' samples was similar (data not shown).

The highest concentration of ^{57}Fe accumulating over 72 h was in the embryos (Fig. 3c), indicating that most of the iron taken up at this stage is partitioned there. Interestingly, the increase in ^{57}Fe enrichment was similar in proximal and distal parts of the grain, suggesting a constant rate of translocation to all grain tissues (Fig. 3c, inset). Overexpression of *TaVIT2* resulted in a

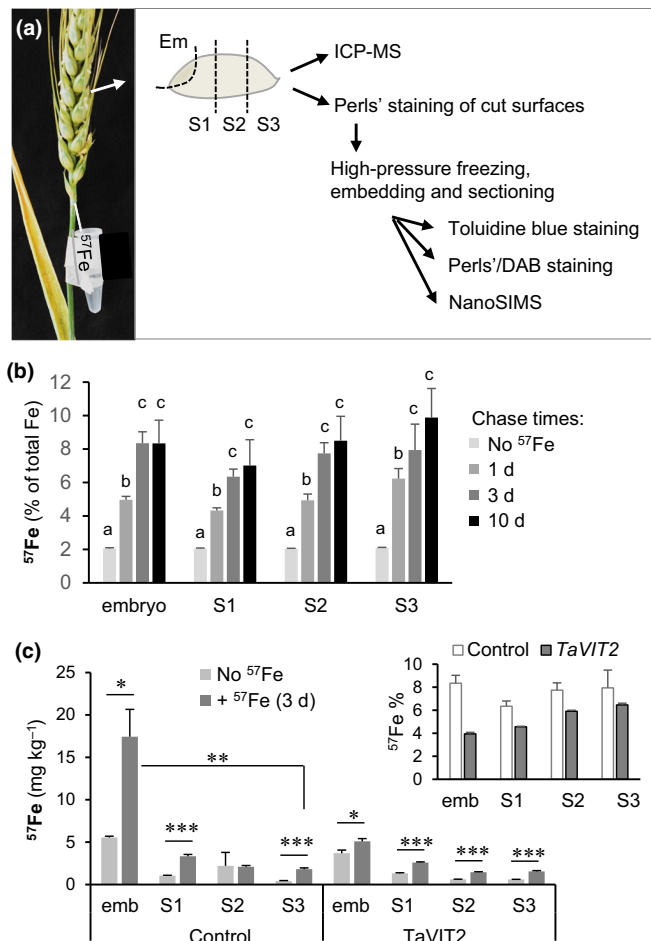


Fig. 3 Iron isotope labelling of developing grain. (a) Diagram of the experimental pipeline for iron-57 (^{57}Fe) feeding and sample preparation. (b) Percentage enrichment of ^{57}Fe in parts of the grain as indicated in (a), following different chase times after pulse-labelling of wheat ears 17–19 d after anthesis. Iron isotopes were quantified by inductively coupled plasma mass spectrometry (ICP-MS). Values are the mean \pm SE of three biological replicates, which are pools of 40 to 50 grain parts from one ear. Letters indicate statistical significance ($P < 0.001$, two-way ANOVA and Tukey's multiple comparisons test). (c) Concentrations of ^{57}Fe in the embryo (emb) and other parts of the grain (see a) in control and in plants overexpressing *TaVIT2* in the endosperm. ICP-MS values are given as absolute numbers and as percentage (inset), and are the mean \pm SE of three biological replicates (see b). *, $P < 0.05$; **, $P < 0.01$; ***, $P < 0.001$ (Student *t*-test).

marked decrease in ^{57}Fe translocation to the embryo (by two-fold), in agreement with the lower total iron concentration of *TaVIT2* embryos (Fig. 1c). There was also a modest decrease in ^{57}Fe translocation to the rest of the grain (Fig. 3c, inset). However, the ^{57}Fe enrichment value in these parts is the sum of iron translocation into the endosperm and aleurone, two tissues with very different iron concentrations. To measure iron translocation into specific grain tissues, the $^{57}\text{Fe} : ^{56}\text{Fe}$ ratio was determined by NanoSIMS, averaging the counts for each isotope over $50 \mu\text{m} \times 50 \mu\text{m}$ regions of interest (ROIs). Wheat samples harvested at 24 h after the start of isotope labelling showed a maximum of 5% enrichment of ^{57}Fe compared to the natural $^{57}\text{Fe} : ^{56}\text{Fe}$

abundance ratio of 2.31%, which was considered too little difference for quantification (data not shown). After labelling for 72 h, up to 20% enrichment of ^{57}Fe was found in ROIs (Fig. 4).

Iron-57 (^{57}Fe) and ^{56}Fe counts from transfer cells, modified aleurone cells, the EAS region, central starchy endosperm, scutellum, embryo plumule and aleurone cells from two different biological replicates were collected and the average ratios are plotted in Fig. 4. In control grain, 12–18% ^{57}Fe enrichment was found in transfer cells, modified aleurone, EAS and the embryo, but only 6–7% ^{57}Fe enrichment in the starchy endosperm and outer aleurone cells. Most tissues in *TaVIT2* grain showed a decrease in $^{57}\text{Fe} : ^{56}\text{Fe}$ relative to control, with a small decrease in the maternal transfer cells and starchy endosperm, but a dramatic decrease in the EAS. At the time point of analysis (21 dpa), lots of iron has already accumulated in the EAS of *TaVIT2* grain, and the low $^{57}\text{Fe} : ^{56}\text{Fe}$ ratio indicates that the diversion into storage organelles has been saturated in this tissue.

Taken together, ^{57}Fe pulse labelling of developing wheat grain, analysed by ICP-MS in grain sectors or by NanoSIMS in specific tissues, therefore revealed a high flux of iron from the maternal transfer cells directly to the embryo, starting well before 21 dpa, which was perturbed by overexpression of *TaVIT2*.

Iron is translocated in dynamic intracellular vesicles

Next, we exploited the combined methods of ^{57}Fe pulse labelling and NanoSIMS to investigate iron dynamics within cells. Previous NanoSIMS analysis of $^{56}\text{Fe}^{16}\text{O}^-$ in durum wheat grains at 16 dpa showed that iron was concentrated in phosphate-containing globoids in the aleurone, whereas it was uniformly distributed in a starchy endosperm cell located $100 \mu\text{m}$ from the aleurone (Moore *et al.*, 2012). Detection of $^{56}\text{Fe}^+$ ions with the O^- beam showed a similar pattern of iron-containing globoids in the aleurone cells of bread wheat at 21 dpa (Figs 5a, S8). Interestingly, ^{57}Fe labelling revealed two populations of iron-dense structures, a population with 20–30% ^{57}Fe enrichment $0.1\text{--}1 \mu\text{m}$ in diameter and a population with *c.* 5% enrichment which were generally larger in diameter ($0.5\text{--}2.5 \mu\text{m}$) (Figs 5b, S8). The first population had virtually no associated PO signal, whereas the second population had a strong PO signal likely derived from phytic acid. In several instances, the ^{57}Fe -rich structures are seen abutting larger globoids and were possibly merging (Fig. 5a, white arrow heads in aleurone image). Overexpression of *TaVIT2* in the endosperm led to a dramatic decrease in ^{57}Fe entering the aleurone between 20 and 22 dpa.

Transfer cells of the nucellar projection connect the vascular bundle from the mother plant to the grain, and thus play an important role in nutrient transport. The pattern of iron-rich bodies was comparable in transfer cells of control and *TaVIT2* grain, showing a combination of disperse iron-rich vesicles and large clusters filling up most of the small cell volume (Figs 6, S9). The percentage ^{57}Fe enrichment was slightly, but non-significantly, decreased in transfer cells of *TaVIT2* grain compared to control (Figs 4, 6), as expected in this maternal tissue through which iron passes before it reaches the grain.

Fe translocation at 24 dpa (late grain filling)

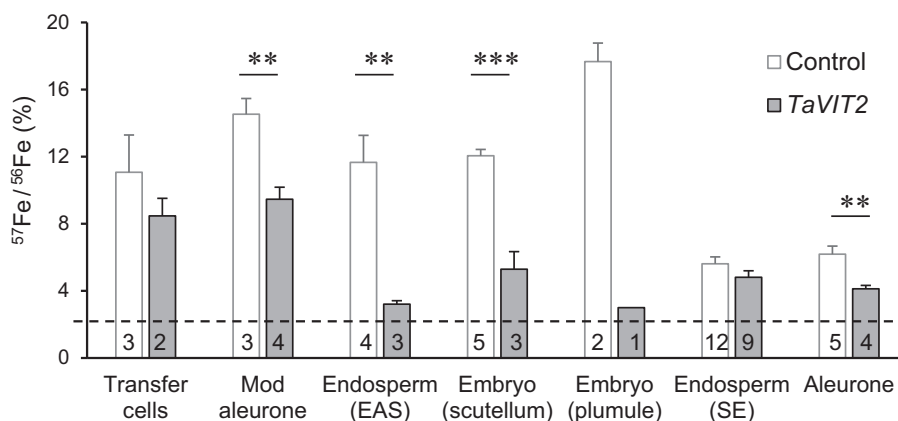


Fig. 4 Iron translocation into different cell types following iron-57 (^{57}Fe) labelling. Ratios of ^{57}Fe and ^{56}Fe signals determined by nanoscale secondary ion mass spectrometry (NanoSIMS), expressed as a percentage, from $50\ \mu\text{m} \times 50\ \mu\text{m}$ regions of interest (ROIs) of different wheat grain tissues. The values are the mean $^{57}\text{Fe} : ^{56}\text{Fe}$ ratio \pm SE of $n \geq 2$ ROIs in two separate wheat plants, except for the embryo plumule of TaVIT2 grain where $n = 1$. The number of ROIs is given in each bar. **, $0.01 < P < 0.001$; ***, $P < 0.001$ (Student *t*-test). The dashed line indicates the naturally occurring $^{57}\text{Fe} : ^{56}\text{Fe}$ ratio (2.3%). dpa, days post anthesis.

In the modified aleurone cells adjacent to the transfer cells, the pattern of iron-rich bodies was different from that in aleurone cells around the periphery of the grain (Figs 5a, 6). Modified aleurone cells in both control and TaVIT2 grain showed an abundance of ^{57}Fe -enriched vesicles, ranging from 6 to 20% enrichment in the control and 6–15% in TaVIT2. These patterns correlate with the specific function of modified aleurone cells, namely nutrient transfer rather than nutrient storage. Endosperm-specific expression of *TaVIT2* did have a negative influence on the iron dynamics in modified aleurone cells, intermediate to the suppression of iron translocation into the maternal transfer cells and EAS.

Starchy endosperm cells between the crease and embryo (EAS) contained only few iron-enriched vesicles 5–7 μm in diameter, whereas cells in the ‘cheeks’ of the developing grain showed a diffuse pattern of iron (Figs 5a, 6). In TaVIT2 grain, large clusters of ^{56}Fe vesicles and globoids were found but with little or no enrichment in ^{57}Fe . It is likely that the cells are saturated with iron before our time point of investigation and that iron transport into the cell is decreased. However, at the periphery of the EAS we observed a cluster of vesicles with smaller, ^{57}Fe -rich vesicles on the outside and larger, Fe + PO containing vesicles towards the centre of the cluster (Fig. 7). Again, instances of abutting vesicles suggest that fusion is taking place, with ‘newer’ ^{57}Fe being delivered to ‘older’ ^{56}Fe stored with PO.

The scutellum contained a large number of iron-rich, membrane-bound vesicles (Fig. 6), in agreement with iron accumulation seen by XRF (Neal *et al.*, 2013; Singh *et al.*, 2013; De Brier *et al.*, 2016). Cells in the outer cell layers of the scutellum, adjacent to endosperm cells that are undergoing programmed cell death, tended to have a higher enrichment with ^{57}Fe . The plumule of the embryo also showed a high density of iron-rich vesicles. In the *TaVIT2* overexpressing grain, the density of the iron vesicles was similar to control grain (Fig. 6), but ^{57}Fe

enrichment was dramatically decreased (Fig. 4), in agreement with the lower total iron content of TaVIT2 embryos (Fig. 3c).

In summary, the presence of iron-rich organelles in most cell types (except the starchy endosperm) and their heterogeneity in ^{57}Fe enrichment suggest that vesicle-mediated transport is a major route of cell-to-cell iron translocation.

Discussion

To gain insight into iron translocation and distribution into developing cereal grains, we developed a protocol for ^{57}Fe labelling combined with NanoSIMS. This revealed how different cell types contribute to iron translocation with remarkable differences in their cell biology. A summary of the findings is presented in Fig. 8. The main flux of iron is from the maternal transfer cells to the embryo through a specific zone of the starchy endosperm, as shown by ^{57}Fe enrichment in embryos of control grain (Fig. 3c) and entrapment of this iron flux when *TaVIT2* is overexpressed under the control of an endosperm-specific promoter (Figs 1–4). A role in nutrient transport for this part of the endosperm, previously termed EAS, has been suggested based on transcriptomics analysis in maize, which showed a marked upregulation of transporters for sugars, amino acids and some metal transporters in this tissue (Doll *et al.*, 2020). The amount of iron travelling to the aleurone layer at the periphery of the endosperm was also strongly affected by *TaVIT2* overexpression (Figs 4, 5), although no iron accumulation was observed in tissues adjacent to the aleurone, and the route of this pool of iron therefore remains unclear.

NanoSIMS analysis of ^{57}Fe provided subcellular detail of how iron is trafficked through the cell by vesicles and vacuolar globoids. Subcellular imaging of ^{57}Fe was facilitated by the recent addition of the RF O-source to the NanoSIMS allowing measurement of positively charged iron ions with discrimination of

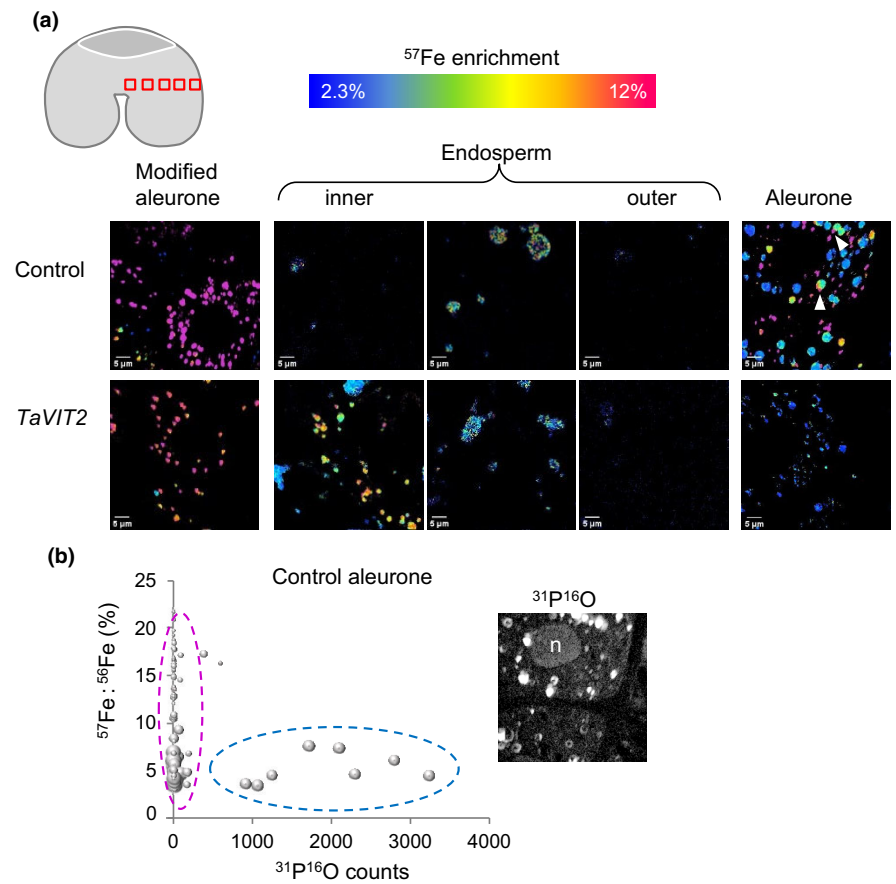


Fig. 5 Nanoscale secondary ion mass spectrometry (NanoSIMS) analysis of iron-57 (^{57}Fe) enrichment along the lateral axis in wheat grain. (a) NanoSIMS scans ($50\ \mu\text{m} \times 50\ \mu\text{m}$) of the indicated tissues in control and TaVIT2 grain. The position of the images is indicated in the cartoon image, top left. The $^{57}\text{Fe} : ^{56}\text{Fe}$ ratio is represented by a colour scale from 2.3 to 12%. For the aleurone cells, the $^{31}\text{P}^{16}\text{O}$ signal is shown in the far-right image in grey scale. Arrow heads indicate possible fusion events of small ^{57}Fe -enriched bodies with larger iron globoids. (b) Relationship between ^{57}Fe enrichment and $^{31}\text{P}^{16}\text{O}$ in iron-dense subcellular structures in aleurone cells of control grain. The size of each data point correlates with the area of the structure. n, nucleus.

$^{57}\text{Fe}^+$ from $^{56}\text{FeH}^+$. By contrast, the negative ^{57}Fe ions could not be resolved with the Cs^+ beam (Fig. S7). The combination of isotope labelling and NanoSIMS is a powerful technique to study dynamic transport processes, including ^{15}N : protein accumulation in wheat grain (Moore *et al.*, 2016), dimethylsulphoniopropionate metabolism using sulphur-34 (^{34}S) in microalgae (Raina *et al.*, 2017) and zinc-70 (^{70}Zn) uptake in radish roots (Ondrasek *et al.*, 2019). Although NanoSIMS cannot determine the precise concentration of ^{57}Fe , the enrichment of ^{57}Fe compared to ^{56}Fe with similar physical properties can be reliably determined, as shown by the small statistical variance between different images of the same tissue and biological replicates (Fig. 4). While our analysis was restricted to one time point in grain development (21 dpa), it nevertheless provided a dynamic snapshot of iron translocation by visualizing the $^{57}\text{Fe} : ^{56}\text{Fe}$ ratio and distinguishing between ‘old’ iron and newly translocated iron.

The small, ^{57}Fe -enriched bodies in the aleurone cells (Fig. 5a) have not previously been observed. The high ^{57}Fe enrichment indicates that this is a pool of iron that has recently entered the cell. Some of the ^{57}Fe -rich bodies appeared to merge with the larger iron-phytate globoids which were also observed by NanoSIMS using the Cs^+ beam (Moore *et al.*, 2012). It is probable that the higher sensitivity achieved by mapping iron as Fe^+ with the O^- beam, rather than FeO^- with the Cs^+ beam, enabled visualization of the small ^{57}Fe -enriched particles, which are low

in PO, and thus contain little phosphate or phytic acid (Fig. 5b). Because free iron is cytotoxic, iron in these small bodies may be bound to citrate or nicotianamine (NA). A pool of iron-citrate was found in aleurone cells of mature wheat grains using X-ray absorption near edge structure (XANES) imaging (De Brier *et al.*, 2016; Pongrac *et al.*, 2020). These studies did not detect iron-NA in aleurone cells and this iron species may only occur during grain filling. At 20 dpa, transcripts of *TaNAS9*, encoding a NA synthase, are abundant in aleurone cells (Fig. S10), which is approximately the same stage as our NanoSIMS analysis. Other techniques such as time-of-flight SIMS analysis of small organic molecules could be used to establish if NA is present in younger grain tissues.

Detection of vesicles enriched in ^{57}Fe in all grain tissues from both control and TaVIT2 grain indicates that iron translocation is predominantly symplastic. Only a small number of NanoSIMS images captured an iron signal in cell walls, see Fig. S11. It is currently unclear how iron is transported through the plant cytosol, although NA is thought to play a key role (Mari *et al.*, 2020). Our study suggests that vesicle transport could also be involved. Vesicle-mediated transport of iron has been reported in erythrocytes, where a large flux of iron is delivered to the mitochondria for haem biosynthesis (Hamdi *et al.*, 2016).

The observed cell-type specific patterns of iron uptake and storage are likely to be underpinned by differential gene

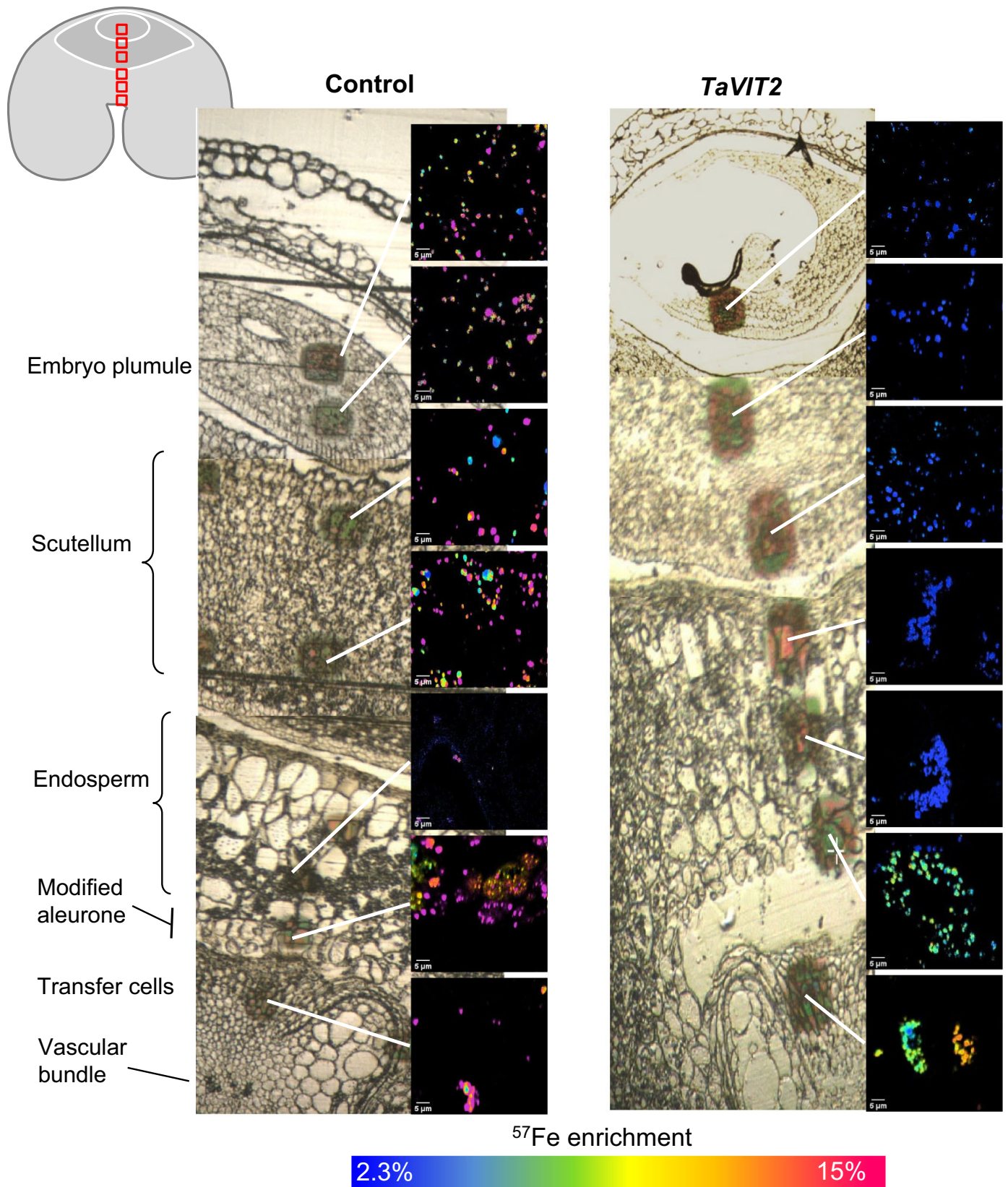


Fig. 6 Nanoscale secondary ion mass spectrometry (NanoSIMS) analysis of iron-57 (^{57}Fe) enrichment along the vertical axis in wheat grain. Light microscopy (LM) images of a transect through a control and a TaVIT2 grain with $50\ \mu\text{m} \times 50\ \mu\text{m}$ images acquired by NanoSIMS showing the $^{57}\text{Fe} : ^{56}\text{Fe}$ ratio. The position of the transect is indicated in the cartoon image, top left. The scan areas appear as dark patches in the LM image. The ^{57}Fe enrichment is represented by a false colour scale from 2.3 to 15%.

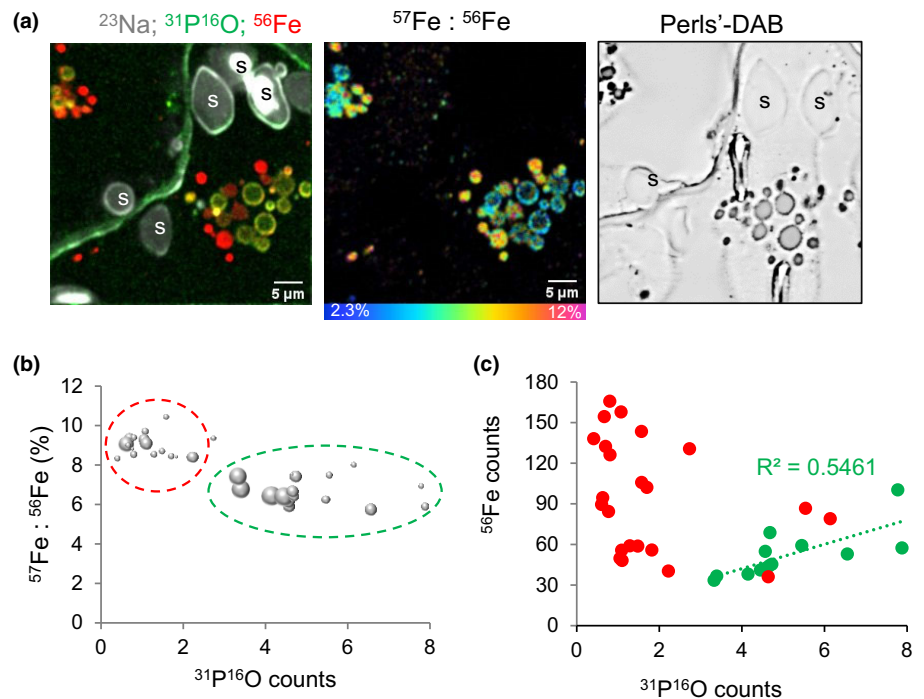


Fig. 7 Heterogeneous composition of iron-rich vesicles. (a) Nanoscale secondary ion mass spectrometry (NanoSIMS) images of endosperm cells at the periphery of the endosperm adjacent to scutellum (EAS) in TaVIT2 grain, showing the distribution of sodium-23 (^{23}Na), $^{31}\text{P}^{16}\text{O}$ and ^{56}Fe (left) and the $^{57}\text{Fe} : ^{56}\text{Fe}$ ratio (middle). The same area in an adjacent $1\ \mu\text{m}$ section stained with Perls'-diamine benzidine (DAB) is shown on the right. A cell wall runs through the middle of the image. s, starch grain. (b) Relationship between the ^{57}Fe enrichment and $^{31}\text{P}^{16}\text{O}$ signal in iron-rich vesicles. The size of each data point corresponds to the area of the vesicle. (c) Relationship between the ^{56}Fe and $^{31}\text{P}^{16}\text{O}$ signal from the iron-rich vesicles.

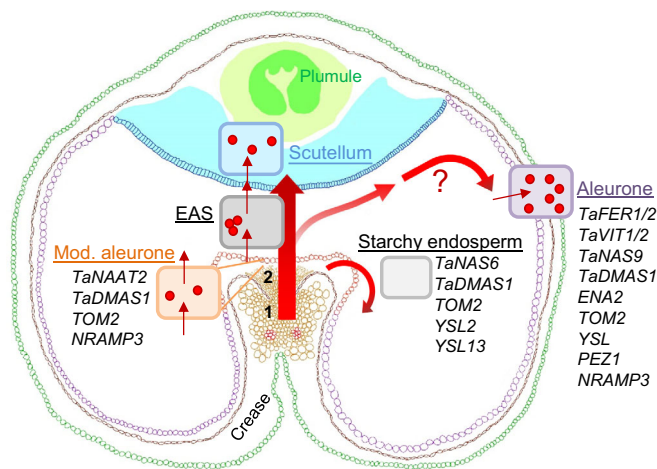


Fig. 8 Proposed model for iron translocation in developing wheat grain. Iron (red arrows and dots) enters the developing grain from the maternal vascular bundle (1) which runs along the ventral crease (perpendicular to the diagram). After exiting the vascular bundle, iron travels through the transfer cells of the nucellar projection (2) and the modified aleurone (orange). The main flux of iron is directly to the scutellum of the embryo, via the endosperm adjacent to the scutellum (EAS). Rounded rectangles depict differentiated cell types, the direction of iron transport in and out of these cells (small arrows), and iron contained in small subcellular bodies (vacuoles or globoids, which are not distinguished here). Transcripts of iron homeostasis genes that are relatively abundant in modified aleurone cells, aleurone cells and starchy endosperm are listed, based on RNA-sequencing data from Pfeifer *et al.* (2014). TaXXX indicates a gene annotated in wheat, *Triticum aestivum*, otherwise the rice acronyms are used.

expression. An RNA-Seq study by Pfeifer *et al.* (2014) investigated gene expression in tissue samples enriched in modified aleurone cells, starchy endosperm and aleurone cells of wheat

grains at 20 dpa. We reanalysed this data set to extract the expression levels of wheat genes likely to be involved in iron homeostasis, based on sequence homology to genes in rice and Arabidopsis (Fig. S10). Ferritin and *VIT* genes were noticeably upregulated in the aleurone tissue, but not in the modified aleurone or starchy endosperm, in agreement with our NanoSIMS data (Fig. 5). Two different *NAS* genes were upregulated in aleurone and starchy endosperm, *TaNAS9* and *TaNAS6*, respectively. *TaNAS9* is orthologous to *OsNAS3* (Bonneau *et al.*, 2016), but there is no direct orthologue of *TaNAS6* in rice. Enzymes encoded by *NAAT* and *DMAS* work sequentially to convert NA to a 3''-oxo intermediate and then to deoxymugineic acid (Beasley *et al.*, 2017). Transcripts of the *TaNAAT2* triad are enriched in the modified aleurone but not in the other two tissues. This suggests that the modified aleurone converts NA to the 3''-oxo intermediate, which could be further converted to deoxymugineic acid by *TaDMAS1* expressed in all three tissues. Wheat homologues of the mugineic acid exporter *OsTOM2* are also expressed in all three tissues, but the homologue of the NA exporter *OsENA2* is primarily expressed in aleurone cells.

Elevated aleurone expression of a wheat gene triad related to *OsPEZ1*, encoding a phenolics exporter active in the xylem (Ishimaru *et al.*, 2011), suggests that enhancing the solubility of iron in cell walls may facilitate iron uptake as well. Uptake of iron-NA complexes is mediated by yellow stripe-like (YSL) transporters, of which seven different paralogues are expressed in the investigated wheat grain tissues. The iron-NA transporter *ZmYSL2* was recently shown to be important for iron import into the embryo and aleurone cells in maize kernels (Zang *et al.*, 2020), and this gene may correspond to *TraesCS2D02G387800* in wheat (Fig. S10c). Transcripts of the wheat homologues of *OsYSL6* and *OsYSL9* are also enriched in

aleurone cells. Interestingly, a rice mutant line of *OsYSL9* had decreased amounts of iron in the embryo, but increased contents in the polished grain (mostly endosperm), indicating that *OsYSL9* plays a role in iron translocation from the EAS to the embryo (Senoura *et al.*, 2017).

Dynamic iron studies, gene expression data and functional genetics will be invaluable for developing new biofortification strategies. Our isotope labelling study indicated that endosperm-specific expression of *TaVIT2* was successful as a biofortification strategy because iron is captured from the large flux going through the EAS and retained there, starting before 20 dpa (Figs 3, 4). Interestingly, previous studies overexpressing ferritin under the same promoter did not lead to accumulation of significant amounts of iron in the endosperm (Neal *et al.*, 2013). A possible reason for this difference is that ferritin is a facultative iron store, which can release iron as easily as taking it up. In *TaVIT2* grain, iron accumulated in a relatively small part of the endosperm, and the challenge will be to direct more iron into the 'cheeks' of the grain. Moreover, increasing total grain iron, rather than redistributing it, would be necessary. It was recently shown that the latter can be achieved by overexpressing the rice *NAS2* gene under the constitutive *UBIQUITIN* promoter (Beasley *et al.*, 2019). Because of different modes of action of the *OsNAS2* and *TaVIT2*, combining these two transgenes is likely to have an additive effect, increasing iron in wholemeal and white flour fractions simultaneously. Moreover, higher NA levels should also raise the concentration of zinc and lead to higher bioavailability of both micronutrients (Beasley *et al.*, 2019). Other genes, such as those encoding grain-specific YSL and PEZ transporters, may also be interesting candidates for biofortification. Isotope labelling and imaging can make an important contribution in understanding cell-specific processes of iron homeostasis, helping to inform such biofortification strategies.

Acknowledgements

The authors would like to thank Kirstie Halsey (Rothamsted Research, Harpenden, UK) for sample preparation for microscopy; Mark Durenkamp (Rothamsted Research) and Graham Chilvers (University of East Anglia, Norwich, UK) for ICP-OES and ICP-MS analyses; Eva Wegel (John Innes Centre, Norwich, UK) for microscopy assistance; Sophie Harrington and Jemima Brinton (John Innes Centre) for help with bioinformatics and Kexue Li for help with NanoSIMS. This research was funded by the Biotechnology and Biological Sciences Research Council, grant awards BB/P019072/1 (SS, YW, JMC, PRS, KLM and JB), BB/T004363/1 (QX), BB/P016855/1 (PRS); and a Royal Society, Newton Fellowship NF171396 to SKV. The NanoSIMS was funded by UK Research Partnership Investment Funding (UKRPIF), Manchester RPIF Round 2. This work was also supported by the Henry Royce Institute for Advanced Materials, funded through Engineering and Physical Sciences Research Council (EPSRC) grants EP/R00661X/1, EP/S019367/1, EP/P025021/1 and EP/P025498/1. Competing interests: none.

Author contributions

SS, YW, EV, SKV, QX, JW and JMC performed experiments and analysed data. JMC, PRS, KLM and JB planned the research. KLM and JB wrote the manuscript.

ORCID

Janneke Balk  <https://orcid.org/0000-0003-4738-1990>
 James M. Connorton  <https://orcid.org/0000-0002-9379-5599>
 Katie L. Moore  <https://orcid.org/0000-0003-1615-7232>
 Peter R. Shewry  <https://orcid.org/0000-0001-6205-2517>
 Eudri Venter  <https://orcid.org/0000-0002-8101-2403>
 Shailender K. Verma  <https://orcid.org/0000-0002-4192-933X>
 Joshua Waites  <https://orcid.org/0000-0001-9899-4557>
 Yongfang Wan  <https://orcid.org/0000-0002-9374-5014>

Data availability

The data that support the findings of this study are available in the Supporting Information of this article and, if not there, available from the corresponding author upon reasonable request.

References

- Bartlett J, Alves S, Smedley M, Snape J, Harwood W. 2008. High-throughput *Agrobacterium*-mediated barley transformation. *Plant Methods* 4: 22.
- Bashir K, Takahashi R, Akhtar S, Ishimaru Y, Nakanishi H, Nishizawa NK. 2013. The knockdown of *OsVIT2* and *MIT* affects iron localization in rice seed. *Rice* 6: 31.
- Beasley JT, Bonneau JP, Johnson AAT. 2017. Characterisation of the nicotianamine aminotransferase and deoxymugineic acid synthase genes essential to Strategy II iron uptake in bread wheat (*Triticum aestivum* L.). *PLoS ONE* 12: e0177061.
- Beasley JT, Bonneau JP, Sánchez-Palacios JT, Moreno-Moyano LT, Callahan DL, Tako E, Glahn RP, Lombi E, Johnson AAT. 2019. Metabolic engineering of bread wheat improves grain iron concentration and bioavailability. *Plant Biotechnology Journal* 17: 1514–1526.
- Bechtel DB, Abecassis J, Shewry PR, Evers AD. 2009. Development, structure, and mechanical properties of the wheat grain. In: Khan K, Shewry PR, eds. *Wheat: chemistry and technology*. Maryland Heights, MO, USA: Elsevier, 51–95.
- Bonneau J, Baumann U, Beasley J, Li Y, Johnson AAT. 2016. Identification and molecular characterization of the nicotianamine synthase gene family in bread wheat. *Plant Biotechnology Journal* 14: 2228–2239.
- Borg S, Brinch-Pedersen H, Tauris B, Holm PB. 2009. Iron transport, deposition and bioavailability in the wheat and barley grain. *Plant and Soil* 325: 15–24.
- Borrill P, Connorton JM, Balk J, Miller AJ, Sanders D, Uauy C. 2014. Biofortification of wheat grain with iron and zinc: Integrating novel genomic resources and knowledge from model crops. *Frontiers Plant Science* 5: 53.
- Bray N, Pimentel H, Melsted P, Pachter L. 2016. Near-optimal probabilistic RNA-seq quantification. *Nature Biotechnology* 34: 525–527.
- De Brier N, Goman SV, Donner E, Paterson D, Smolders E, Delcours JA, Lombi E. 2016. Element distribution and iron speciation in mature wheat grains (*Triticum aestivum* L.) using synchrotron X-ray fluorescence microscopy mapping and X-ray absorption near-edge structure (XANES) imaging. *Plant, Cell & Environment* 39: 1835–1847.
- Che J, Yamaji N, Ma J. 2021. Role of a vacuolar iron transporter *OsVIT2* in the distribution of iron to rice grains. *New Phytologist* 230: 1049–1062.

- Cominelli E, Pilu R, Sparvoli F. 2020. Phytic acid and mineral biofortification strategies: from plant science to breeding and biotechnological approaches. *Plants (Basel)* 9: 553.
- Connorton JM, Jones ER, Rodríguez-Ramiro I, Fairweather-Tait S, Uauy C, Balk J. 2017. Wheat vacuolar iron transporter TaVIT2 transports Fe and Mn and is effective for biofortification. *Plant Physiology* 174: 2434–2444.
- Detterbeck A, Pongrac P, Persson DP, Vogel-mikus K, Kelemen M, Husted S, Schjoerring JK, Vavpetic P, Pelicon P, Arc I *et al.* 2020. Temporal and spatial patterns of zinc and iron accumulation during barley (*Hordeum vulgare* L.) grain development. *Journal of Agricultural and Food Chemistry* 68: 12229–12240.
- Doll NM, Just J, Brunaud V, Căiuş J, Grimault A, Depège-Fargeix N, Esteban E, Pasha A, Provart NJ, Ingram GC *et al.* 2020. Transcriptomics at maize embryo/endosperm interfaces identifies a transcriptionally distinct endosperm subdomain adjacent to the embryo scutellum. *Plant Cell* 32: 833–852.
- Engelke DR, Krikos A, Bruck ME, Ginsburg D. 1990. Purification of *Thermus aquaticus* DNA polymerase expressed in *Escherichia coli*. *Analytical Biochemistry* 191: 396–400.
- Evers AD. 1970. Development of the endosperm of wheat. *Annals of Botany* 34: 547–555.
- Garnett TP, Graham RD. 2005. Distribution and remobilization of iron and copper in wheat. *Annals of Botany* 95: 817–826.
- Grovenor CRM, Smart KE, Kilburn MR, Shore B, Dilworth JR, Martin B, Hawes C, Rickaby REM. 2006. Specimen preparation for NanoSIMS analysis of biological materials. *Applied Surface Science* 252: 6917–6924.
- Hamdi A, Roshan TM, Kahawita TM, Mason AB, Sheftel AD, Ponka P. 2016. Erythroid cell mitochondria receive endosomal iron by a “kiss-and-run” mechanism. *Biochimica et Biophysica Acta (BBA) – Molecular Cell Research* 1863: 2859–2867.
- Hayta S, Smedley MA, Demir SU, Blundell R, Hinchliffe A, Atkinson N, Harwood WA. 2019. An efficient and reproducible *Agrobacterium*-mediated transformation method for hexaploid wheat (*Triticum aestivum* L.). *Plant Methods* 15: 121.
- Hoppe P, Cohen S, Meibom A. 2013. Technical aspects and applications in cosmochemistry and biological geochemistry. *Geostandards and Geoanalytical Research* 37: 111–154.
- Ishimaru Y, Kakei Y, Shimo H, Bashir K, Sato Y, Sato Y, Uozumi N, Nakanishi H, Nishizawa NK. 2011. A rice phenolic efflux transporter is essential for solubilizing precipitated apoplasmic iron in the plant stele. *Journal of Biological Chemistry* 286: 24649–24655.
- Iwai T, Takahashi M, Oda K, Terada Y, Yoshida KT. 2012. Dynamic changes in the distribution of minerals in relation to phytic acid accumulation during rice seed development. *Plant Physiology* 160: 2007–2014.
- Kim SA, Punshon T, Lanzirotti A, Li L, Alonso JM, Ecker JR, Kaplan J, Guerinet ML. 2006. Localization of iron in Arabidopsis seed requires the vacuolar membrane transporter VIT1. *Science* 314: 1295–1298.
- Kopittke PM, Lombi E, van der Ent A, Wang P, Laird JS, Moore KL, Persson DP, Husted S. 2020. Methods to visualize elements in plants. *Plant Physiology* 182: 1869–1882.
- Lamacchia C, Shewry PR, Di Fonzo N, Forsyth JL, Harris N, Lazzeri PA, Napier JA, Halford NG, Barcelo P. 2001. Endosperm-specific activity of a storage protein gene promoter in transgenic wheat seed. *Journal of Experimental Botany* 52: 243–250.
- Malherbe J, Penen F, Isaure MP, Frank J, Hause G, Dobritsch D, Gontier E, Horréard F, Hillion F, Schaumlöffel D. 2016. A new radio frequency plasma oxygen primary ion source on nano secondary ion mass spectrometry for improved lateral resolution and detection of electropositive elements at single cell level. *Analytical Chemistry* 88: 7130–7136.
- Mari S, Bailly C, Thomine S. 2020. Handing off iron to the next generation: how does it get into seeds and what for? *Biochemical Journal* 477: 259–274.
- Meguro R, Asoano Y, Odagiri S, Li C, Iwatsuki H, Shoumura K. 2007. Nonheme-iron histochemistry for light and electron microscopy: a historical, theoretical and technical review. *Archives of Histology and Cytology* 70: 1–19.
- Moore KL, Tosi P, Palmer R, Hawkesford MJ, Grovenor CRM, Shewry PR. 2016. The dynamics of protein body formation in developing wheat grain. *Plant Biotechnology Journal* 14: 1876–1882.
- Moore KL, Zhao F-J, Gritsch CS, Tosi P, Hawkesford MJ, McGrath SP, Shewry PR, Grovenor CRM. 2012. Localisation of iron in wheat grain using high resolution secondary ion mass spectrometry. *Journal of Cereal Science* 55: 183–187.
- Neal AL, Geraki K, Borg S, Quinn P, Mosselmans JF, Brinch-Pedersen H, Shewry PR. 2013. Iron and zinc complexation in wild-type and ferritin-expressing wheat grain: Implications for mineral transport into developing grain. *Journal of Biological Inorganic Chemistry* 18: 557–570.
- Olsen OA. 2020. The modular control of cereal endosperm development. *Trends in Plant Science* 25: 279–290.
- Ondrasek G, Rengel Z, Clode PL, Kilburn MR, Guagliardo P, Romic D. 2019. Zinc and cadmium mapping by NanoSIMS within the root apex after short-term exposure to metal contamination. *Ecotoxicology and Environmental Safety* 171: 571–578.
- Pfeifer K, Kugler K, Sandve S, Zhan B, Rudi H, Hvidsten T, Meyer K, Olsen O. 2014. Genome interplay in the grain transcriptome of hexaploid bread wheat. *Science* 345: 1250091.
- Pongrac P, Arčon I, Castillo-Michel H, Vogel-mikuš K. 2020. Mineral element composition in grain of awned and awnleted wheat (*Triticum aestivum* L.) cultivars: tissue-specific iron speciation and phytate and non-phytate ligand ratio. *Plants* 9: 79.
- Pottier M, Dumont J, Masclaux-Daubresse C, Thomine S. 2019. Autophagy is essential for optimal translocation of iron to seeds in Arabidopsis. *Journal of Experimental Botany* 70: 845–858.
- Raina JB, Clode PL, Cheong S, Bougoure J, Kilburn MR, Reeder A, Forêt S, Stat M, Beltran V, Thomas-Hall P *et al.* 2017. Subcellular tracking reveals the location of dimethylsulfoniopropionate in microalgae and visualises its uptake by marine bacteria. *eLife* 6: e23008.
- Roschzttardtz H, Conéjéro G, Curie C, Mari S. 2009. Identification of the endodermal vacuole as the iron storage compartment in the Arabidopsis embryo. *Plant Physiology* 151: 1329–1338.
- Senoura T, Sakashita E, Kobayashi T, Takahashi M, Aung MS, Masuda H, Nakanishi H, Nishizawa NK. 2017. The iron-chelate transporter OsYSL9 plays a role in iron distribution in developing rice grains. *Plant Molecular Biology* 95: 375–387.
- Singh SP, Vogel-Mikuš K, Arčon I, Vavpetić P, Jeromel L, Pelicon P, Kumar J, Tuli R. 2013. Pattern of iron distribution in maternal and filial tissues in wheat grains with contrasting levels of iron. *Journal of Experimental Botany* 64: 3249–3260.
- Takahashi M, Nozoye T, Kitajima N, Fukuda N, Hokura A, Terada Y, Nakai I, Ishimaru Y, Kobayashi T, Nakanishi H *et al.* 2009. In vivo analysis of metal distribution and expression of metal transporters in rice seed during germination process by microarray and X-ray fluorescence imaging of Fe, Zn, Mn, and Cu. *Plant and Soil* 325: 39–51.
- Uauy C, Distelfeld A, Fahima T, Blechl A, Dubcovsky J. 2006. A NAC gene regulating senescence improves grain protein, zinc, and iron content in wheat. *Science* 314: 1298–1301.
- Vasconcelos MW, Gruissem W, Bhullar NK. 2017. Iron biofortification in the 21st century: setting realistic targets, overcoming obstacles, and new strategies for healthy nutrition. *Current Opinion in Biotechnology* 44: 8–15.
- Wang Q, Zang Y, Zhou X, Xiao W. 2017. Characterization of four rice *UEV1* genes required for Lys63-linked polyubiquitination and distinct functions. *BMC Plant Biology* 17: 126.
- Waters BM, Uauy C, Dubcovsky J, Grusak MA. 2009. Wheat (*Triticum aestivum*) NAM proteins regulate the translocation of iron, zinc, and nitrogen compounds from vegetative tissues to grain. *Journal of Experimental Botany* 60: 4263–4274.
- WHO. 2013. *Research for universal health coverage*. [WWW document] URL www.WHO.int/whr/2013/report/en/ [accessed 27 April 2021].
- WHO. 2015. *The global prevalence of anaemia in 2011*. [WWW document] URL www.WHO.int/nutrition/publications/micronutrients/global_prevalence_anemia_2011/en/ [accessed 27 April 2021].
- Wu L, Di DW, Zhang D, Song B, Luo P, Guo GQ. 2015. Frequent problems and their resolutions by using thermal asymmetric interlaced PCR (TAIL-PCR) to clone genes in Arabidopsis T-DNA tagged mutants. *Biotechnology and Biotechnological Equipment* 29: 260–267.

Zang J, Huo Y, Liu J, Zhang H, Liu J, Chen H. 2020. Maize YSL2 is required for iron distribution and development in kernels. *Journal of Experimental Botany* 71: 5896–5910.

Zhang Y, Xu YH, Yi HY, Gong JM. 2012. Vacuolar membrane transporters OsVIT1 and OsVIT2 modulate iron translocation between flag leaves and seeds in rice. *The Plant Journal* 72: 400–410.

Supporting Information

Additional Supporting Information may be found online in the Supporting Information section at the end of the article.

Fig. S1 Insertion site of the T-DNA in line 22-19.

Fig. S2 Germination of TaVIT2 grain is similar to control grain.

Fig. S3 Manganese, zinc and phosphorus in pearling fractions of wheat grain.

Fig. S4 Additional images of enhanced Perls' staining of TaVIT2 grain.

Fig. S5 TEM and EDS analysis of TaVIT2 grain.

Fig. S6 Expression pattern of the *HMW-TaVIT2* transgene.

Fig. S7 NanoSIMS data from the iron standard.

Fig. S8 NanoSIMS images and chemical iron staining of aleurone cells.

Fig. S9 NanoSIMS images 50 $\mu\text{m} \times 50 \mu\text{m}$ of transfer cells.

Fig. S10 Transcript abundance of iron homeostasis genes in selected wheat grain tissues.

Fig. S11 NanoSIMS images of iron in cell walls.

Methods S1 Additional information on Materials and Methods.

Table S1 Copy number analysis and iron concentration in white flour of *HMW-TaVIT2* wheat lines.

Table S2 Oligonucleotides used in this study.

Please note: Wiley Blackwell are not responsible for the content or functionality of any Supporting Information supplied by the authors. Any queries (other than missing material) should be directed to the *New Phytologist* Central Office.



About *New Phytologist*

- *New Phytologist* is an electronic (online-only) journal owned by the New Phytologist Foundation, a **not-for-profit organization** dedicated to the promotion of plant science, facilitating projects from symposia to free access for our Tansley reviews and Tansley insights.
- Regular papers, Letters, Viewpoints, Research reviews, Rapid reports and both Modelling/Theory and Methods papers are encouraged. We are committed to rapid processing, from online submission through to publication 'as ready' via *Early View* – our average time to decision is <26 days. There are **no page or colour charges** and a PDF version will be provided for each article.
- The journal is available online at Wiley Online Library. Visit **www.newphytologist.com** to search the articles and register for table of contents email alerts.
- If you have any questions, do get in touch with Central Office (np-centraloffice@lancaster.ac.uk) or, if it is more convenient, our USA Office (np-usaoffice@lancaster.ac.uk)
- For submission instructions, subscription and all the latest information visit **www.newphytologist.com**